Microscopic determination of macroscopic boundary conditions in Newtonian liquids

Hiroyoshi Nakano and Shin-ichi Sasa
Department of Physics, Kyoto University, Kyoto 606-8502, Japan

(Received 21 August 2018; published 14 January 2019)

We study boundary conditions applied to the macroscopic dynamics of Newtonian liquids from the view of microscopic particle systems. We assume the existence of microscopic boundary conditions that are uniquely determined from a microscopic description of the fluid and the wall. By using molecular dynamical simulations, we examine a possible form of the microscopic boundary conditions. In the macroscopic limit, we may introduce a scaled velocity field by ignoring the higher-order terms in the velocity field that is calculated from the microscopic boundary condition and standard fluid mechanics. We define macroscopic boundary conditions as the boundary conditions that are imposed on the scaled velocity field. The macroscopic boundary conditions contain a few phenomenological parameters for an amount of slip, which are related to a functional form of the given microscopic boundary condition. By considering two macroscopic limits of the nonequilibrium steady state, we propose two different frameworks for determining macroscopic boundary conditions.

DOI: 10.1103/PhysRevE.99.013106

I. INTRODUCTION

Over the past two decades boundary conditions on solid surfaces have been a focus of study in the field of fluid dynamics [1–4]. This focus stems from the remarkable developments of experimental techniques for nano- and microscale systems showing the breakdown of the stick boundary condition, specifically, that a fluid at a solid surface has no velocity relative to it [5–20]. Even Newtonian liquids slip on a solid surface and the boundary condition is far more complicated than conventionally thought. From improvements in experimental techniques and developments in molecular dynamical simulations, many possible boundary conditions for Newtonian liquids have been discovered [21–41]. The question "What is the most appropriate boundary condition of Newtonian liquids at solid surfaces?" has attracted a great deal of attention because of its fundamental physical interests and practicality in small-scale fluid dynamics. However, there are only a few attempts at studying the boundary condition from the perspective of microscopic physical laws. When we consider the next application of these experimental and numerical results, it is important to give a microscopic foundation of the boundary condition and comprehensively organize these results.

Since the 19th century, the possibility of the breakdown of the stick boundary condition has been discussed. At the center of this discussion, the partial slip boundary condition and the slip length were introduced by Navier [42]. In the partial slip boundary condition the slip velocity of the fluid at the wall v_s is linearly proportional to the shear rate at the wall $\dot{\gamma}$ as [43–45]

$$v_s = b\dot{\gamma}, \tag{1}$$

where the proportionality constant b is the slip length. The slip length represents the distance at which the fluid velocity extrapolates to zero beyond the surface of the wall. In Navier's partial slip boundary condition, it is assumed that the slip length does not depend on the shear rate [42,46]. By the mid-20th century, the slip length had not been experimentally confirmed and the stick boundary condition had been applied successfully to quantitatively explain numerous macroscopic experiments [43,47]. However, in the 21st century, sensitive and sophisticated numerical simulations and laboratory experiments of Newtonian liquids in confined geometries have revealed the existence of the slip length and, as a result, the Navier's partial slip boundary condition has been recognized as a more appropriate and practical boundary condition [4,21,25,26,29,30]. Much effort has been devoted to the investigation of factors affecting the slip length such as surface roughness [36,48–53] and wettability [4,54,55].

Further intensive research have discovered the shear dependence of the slip length. The shear-rate-dependent slip was initially intimated in computer simulations at high shear rates [37–41] and was reported in laboratory experiments [19,23,24,27]. These studies indicate that the slip length is independent of the shear rate only when the shear rate is small enough [34].

Based on these achievements, research on boundary conditions is expected to move to a new stage. The shear dependence of the slip length is obviously a breakdown of Navier's partial slip boundary condition. As advances in experimental techniques replaced the stick boundary condition with Navier's partial slip boundary condition as the fundamental boundary condition, more advanced experimental technique will replace Navier's partial slip boundary condition with a more fundamental boundary condition. At this time, the microscopic foundation of boundary conditions is of practical importance. Thus, the first problem we are tasked with is "to determine the microscopic boundary condition from the viewpoint of microscopic particle systems."

Here, even if we obtain a microscopic boundary condition, the boundary conditions we conventionally used for a macroscopic description are still worthwhile. Such macroscopic boundary conditions have been applied to obtain satisfactory

results from the macroscopic point of view in many situations. Therefore, whenever we impose an extent of the measurement accuracy from the macroscopic point of view, the system can be characterized by the macroscopic boundary condition rather than the microscopic boundary condition. We should define this measurement accuracy as a mathematical concept so that we can connect the macroscopic boundary condition with the microscopic boundary condition. Thus, the second problem we tackle is "to derive the macroscopic boundary conditions from the microscopic boundary condition by formulating proper macroscopic limits."

In this paper, we propose a framework to organize the macroscopic boundary conditions for a simple case, specifically, uniform shear flow. The starting point should be the microscopic boundary condition. Since it is unknown, we first introduce a tentative fundamental boundary condition that is consistent with results obtained previously in numerical simulations and laboratory experiments. For this purpose, we use molecular dynamical simulation. Then we introduce the measurement accuracy in the uniform shear flow as a mathematical concept. By using this framework, we discuss what kind of boundary conditions should be used in a given situation.

The key idea is to introduce a relation between the measurement accuracy and the system-size dependence of the velocity fields in the infinite volume limit of the uniform shear flow. By ignoring the higher terms of the velocity fields in the system size, we formulate the measurement accuracy. Then we can obtain the macroscopic boundary condition that satisfies the required measurement accuracy. We notice that the macroscopic boundary conditions depend on the choice of the infinite volume limit of the uniform shear flow and the order of terms to be left. We develop two different frameworks of the macroscopic boundary conditions by considering two different infinite volume limits of the uniform shear flow.

The remainder of this paper is organized as follows. In Sec. II, the setup of our model is introduced. We explain the problems to be studied in this paper in terms of our setup. In Sec. III, we describe the determination of the microscopic boundary condition by using the molecular dynamical simulations. In Sec. IV, we determine the macroscopic boundary conditions based on the microscopic boundary condition. The Secs. V and VI are devoted to a brief summary and discussion.

II. SETUP AND QUESTION

A. Model

We introduce a model for studying boundary conditions for fluid dynamics. A schematic illustration is shown in Fig. 1. The fluid consists of N particles that are confined to an $L_x \times L_y \times L_z$ cubic box. We impose periodic boundary conditions along the x and y directions and introduce two parallel walls so as to confine particles in the z direction. We represent the two walls as potential forces acting on the particles. Let $(\boldsymbol{r}_i, \boldsymbol{p}_i)$, $(i = 1, 2, \ldots, N)$, be the position and momentum of the ith particle. The Hamiltonian of the system is given by

$$H = \sum_{i=1}^{N} \frac{\boldsymbol{p}_i^2}{2m} + U\left[(\boldsymbol{r}_i)_{i=1}^N\right] \tag{2}$$

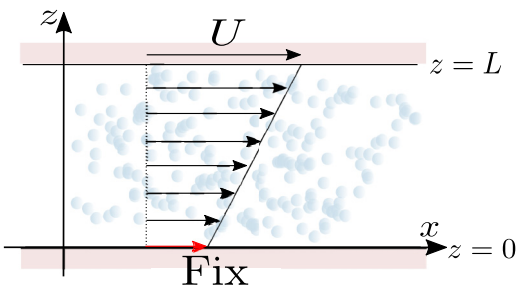

FIG. 1. Schematic illustration of our model.

with

$$U\left[(\boldsymbol{r}_i)_{i=1}^N\right] \equiv \sum_{i<j} V_{\mathrm{FF}}(|\boldsymbol{r}_i - \boldsymbol{r}_j|) + \sum_{i=1}^{N} U_{\mathrm{BW}}(\boldsymbol{r}_i) + \sum_{i=1}^{N} U_{\mathrm{TW}}(\boldsymbol{r}_i). \tag{3}$$

$V_{\mathrm{FF}}(r)$ describes an interaction potential between two particles. $U_{\mathrm{BW}}(\boldsymbol{r})$ and $U_{\mathrm{TW}}(\boldsymbol{r})$ represent a $z = 0$ wall potential and a $z = L_z$ wall potential, respectively. In region B near the $z = L_z$ wall, which is given by $[0, L_x] \times [0, L_y] \times [L, L_z]$, we apply the Langevin thermostat and the external force f along the x axis. We assume that $U_{\mathrm{TW}}(\boldsymbol{r})$ has nonzero value only in region B. Then, the particles obey the Langevin equation

$$m\frac{d^2 r_i^\alpha}{dt^2} = -\sum_{j(\neq i)} \frac{\partial V_{\mathrm{FF}}(|\boldsymbol{r}_i - \boldsymbol{r}_j|)}{\partial r_i^\alpha} - \sum_{i=1}^{N} \frac{\partial U_{\mathrm{BW}}(\boldsymbol{r}_i)}{\partial r_i^\alpha} \tag{4}$$

for $z \in [0, L]$, and

$$m\frac{d^2 r_i^\alpha}{dt^2} = -\sum_{j(\neq i)} \frac{\partial V_{\mathrm{FF}}(|\boldsymbol{r}_i - \boldsymbol{r}_j|)}{\partial r_i^\alpha} - \sum_{i=1}^{N} \frac{\partial U_{\mathrm{TW}}(\boldsymbol{r}_i)}{\partial r_i^\alpha} + f^\alpha - \zeta \frac{dr_i^\alpha}{dt} + \xi_i^\alpha(t) \tag{5}$$

for $z \in [L, L_z]$, where $\boldsymbol{f} = (f, 0, 0)$, $\boldsymbol{\xi}_i$ represents thermal noise satisfying

$$\left\langle \xi_i^\alpha(t)\xi_j^\beta(t')\right\rangle = 2\zeta k_B T \delta_{ij}\delta^{\alpha\beta}\delta(t - t'), \tag{6}$$

where k_B is the Boltzmann constant, T the temperature of the thermostat, and ζ the friction coefficient.

B. Observed quantity

We concentrate on the velocity vector field and stress tensor field in the steady state. This subsection summarizes the definition of these quantities. Let $\hat{\rho}(\boldsymbol{r}; \Gamma_t)$, $\hat{\pi}^a(\boldsymbol{r}; \Gamma_t)$, and $\hat{J}^{ab}(\boldsymbol{r}; \Gamma_t)$ denote the microscopic mass density, momentum density and momentum current density at a given point $\boldsymbol{r}$, respectively, for a given microscopic configuration $\Gamma_t \equiv [\boldsymbol{r}_1(t), \ldots, \boldsymbol{r}_N(t), \boldsymbol{p}_1(t), \ldots, \boldsymbol{p}_N(t)]$ at time t; see Appendix A for details of these definitions. We consider the temporal and spatial average of these microscopic fields. In particular, we consider the z dependence of the averaged local quantities. We perform spatial average in the slab with bin width Δz at the center z and temporal average for a time

interval τ in the steady state. For example, the averaged mass density at any z is given by

$$\rho(z) = \langle\hat{\rho}(z)\rangle_{\rm ss} = \frac{1}{\tau}\int_0^\tau dt \frac{1}{L_x L_y}\int_0^{L_x} dx \int_0^{L_y} dy \times \frac{1}{\Delta z}\int_{z-\Delta z/2}^{z+\Delta z/2} dz \hat{\rho}(\boldsymbol{r};\Gamma_t), \tag{7}$$

where the system is assumed to be in steady state at $t = 0$. Similarly, we give the averaged momentum density $\pi^a(z)$ and momentum current $J^{ab}(z)$. Then, we define velocity $v^a(z)$ and stress $\sigma^{ab}(z)$ at z as

$$v^a(z) = \frac{\pi^a(z)}{\rho(z)}, \tag{8}$$

$$\sigma^{ab}(z) = -J^{ab}(z) + \rho(z)v^a(z)v^b(z). \tag{9}$$

We assume that the velocity field is parallel to the x direction sufficiently far away from the wall. We focus on $v^x(z)$ and $\sigma^{xz}(z)$.

C. Problem

This subsection explains the problem to be studied in the remainder of this paper in terms of the quantities defined above.

We refer to the region sufficiently far from the walls as the bulk. Our chief concern is the velocity and stress profiles $(v^x(z), \sigma^{xz}(z))$ of the bulk in the steady state. Fluid mechanics is the theory for describing the macroscopic behaviors of these quantities. For our setup, the constitutive equation is given by

$$\sigma^{xz} = \eta\frac{dv^x}{dz} \tag{10}$$

except for a region near the walls, where η is a dynamical viscous coefficient. Then, we extrapolate the velocity field in the bulk to the whole region $[0, L_x] \times [0, L_y] \times [0, L]$ while retaining the relation (10). Let the extrapolated velocity at $z = L$ be given by

$$v^x(L) = U. \tag{11}$$

Since we obtain any U by controlling the external force f in our setup, we may treat U as a parameter. Then we focus on the boundary condition at the $z = 0$ wall. Because forces are balanced in the steady state, the shear stress is independent of the z coordinate:

$$\sigma^{xz}(z) = \sigma^{xz} = \text{const.} \tag{12}$$

From (10), (11), and (12), we characterize the extrapolated velocity field by

$$v^x(z) = \frac{\sigma^{xz}}{\eta}(z - L) + U, \tag{13}$$

where η is assumed to be known. When we observe stress σ^{xz}, we obtain the extrapolated velocity field by using (13) with η and U. Thus, if a boundary condition determines the extrapolated velocity field $v^x(z)$, the boundary condition should be related to σ^{xz}, which we express as $\sigma^{xz}(U)$ with η fixed. We emphasize that we study the extrapolated velocity field instead of the real velocity field, because our main concern is $(v^x(z), \sigma^{xz}(z))$ in the bulk, and not the real velocity field near the walls. Hereafter, for simplicity, we refer to the extrapolated velocity field as the velocity field.

We remark that the boundary condition may depend on the measurement accuracy or the scale of interest. For example, there is a case that finite $|v^x(0)|$ cannot be observed for a given accuracy in an investigation for a phenomenon. $\sigma^{xz}(U)$ should be determined in accordance with the required accuracy of $v^x(z)$. We refer to such boundary conditions as the macroscopic boundary condition. Moreover, it is reasonable to conjecture that there is a boundary condition determined only by the microscopic setup, independent of the scale of interest. If we demand greater accuracy in $v^x(z)$, then we should use this microscopic boundary condition. In this paper, we explore the most appropriate microscopic boundary condition and study the macroscopic boundary condition based on the appropriate condition.

III. MOLECULAR DYNAMICAL SIMULATION

A. Preliminaries

We perform numerical simulations with the following potentials in (3). First, the interaction between two particles $V_{\rm FF}(r)$ is given by the truncated Lennard-Jones potential with a cut-off length r_c:

$$V_{\rm FF}(r) \equiv 4\epsilon\left[\left(\frac{\sigma}{r}\right)^{12} - c\left(\frac{\sigma}{r}\right)^6 + C_{\rm FF}^{(2)}r^2 + C_{\rm FF}^{(0)}\right] \tag{14}$$

for $r < r_c$ and $V_{\rm FF}(r) = 0$ otherwise. $C_{\rm FF}^{(2)}$ and $C_{\rm FF}^{(0)}$ are determined by the condition $V_{\rm FF}(r_c) = 0$ and $V'_{\rm FF}(r_c) = 0$ [56]. Second, the $z = 0$ wall consists of N_w material points, which are fixed on the square lattice in the $z = 0$ plane. The lattice constant is denoted by a. Let $\boldsymbol{q}_i$ $(i = 1, 2, \ldots, N_w)$ be the position of the material points. The interaction potential between a material point and a fluid particle $V_{\rm BW}(r)$ is given by the same form as (14) with $\epsilon_{\rm BW}$, $\sigma_{\rm BW}$ and $c_{\rm BW}$. Then, $U_{\rm BW}(\boldsymbol{r})$ is expressed by

$$U_{\rm BW}(\boldsymbol{r}) \equiv \sum_{j=1}^{N_w} V_{\rm BW}(|\boldsymbol{r} - \boldsymbol{q}_j|), \tag{15}$$

where $\sigma_{\rm BW}$ is given by

$$\sigma_{\rm BW} \equiv \frac{a + \sigma}{2} \tag{16}$$

so that the lattice constant a is treated as the diameter of the particles constituting the $z = 0$ wall. Finally, the potential between the $z = L_z$ wall and a fluid particle is given by

$$U_{\rm TW}(\boldsymbol{r}) = 4\epsilon_{\rm TW}\left[\left(\frac{\sigma_{\rm TW}}{L_z - z}\right)^{12} - \left(\frac{\sigma_{\rm TW}}{L_z - z}\right)^6 + C_{\rm TW}^{(2)}(L_z - z)^2 + C_{\rm TW}^{(0)}\right] \tag{17}$$

for $z > L_z - r_c$; otherwise, $U_{\rm TW}(\boldsymbol{r}) = 0$.

In numerical simulations, all the quantities are converted to dimensionless forms by setting $m = \sigma = \epsilon = 1$. We fix $L_x = 30.0\sigma$, $L_y = 30.0\sigma$, $L_z = 24.0\sigma$, and $L = 20.0\sigma$. The particle number is set to $N = 16200$, which corresponds to particle number density $\rho = 0.75\sigma^{-3}$. The temperature and

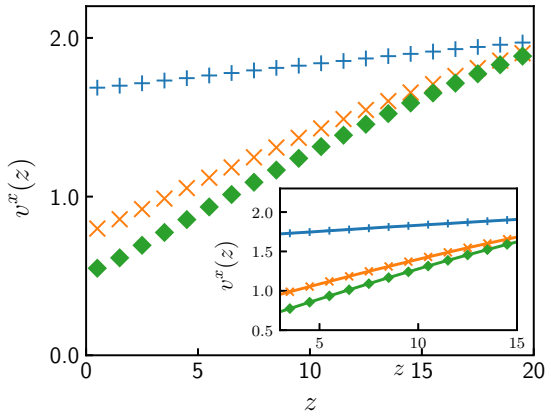

FIG. 2. Velocity profiles for the applied force $f = 2.0$. The wall parameters are chosen as $(a, c_{\mathrm{BW}}) = (0.5, 0.6)$ (blue), (0.6,1.0) (orange), and (0.7,1.0) (green). Inset: linear fits of the velocity profile away from the walls.

the friction coefficient of the Langevin thermostat are set to $k_B T/\epsilon = 1.1$ and $\zeta = 1.0\sqrt{\epsilon m}/\sigma$, respectively. The potential parameters are fixed to $c = 1.0$, $\epsilon_{\mathrm{TW}}/\epsilon = \epsilon_{\mathrm{BW}}/\epsilon = 0.6$, and $\sigma_{\mathrm{TW}}/\sigma = 1.0$. The cutoff distance is set to $r_c = 2.5\sigma$. Then, we characterize the $z = 0$ wall by the value of a and c_{BW}.

B. Microscopic boundary condition

We study the behavior near the $z = 0$ wall. Figure 2 shows examples of the velocity profile in the steady state, with $f = 2.0$ and $(a, c_{\mathrm{BW}}) = (0.5, 0.6)$, $(0.6, 1.0)$, and $(0.7, 1.0)$. The velocity profiles in $3 \leqslant z \leqslant 15$ (inset of Fig. 2) are well fitted linearly. This suggests that uniform shear flow appears in the region $3 \leqslant z \leqslant 15$. Therefore, we identify this region with the bulk. Figure 3 shows the shear stress as a function of shear rate in the bulk. From Fig. 3, we find that (10) holds and η is independent of wall parameters. We note that η is independent of the shear rate in the shear rate range used in this paper.

We consider the boundary condition at $z = 0$ that is consistent with the velocity profiles measured above. The

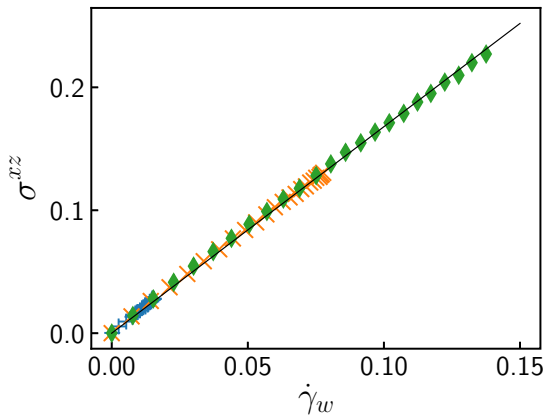

FIG. 3. Stress tensor as a function of shear rate. The applied force f is varied from 0.2 to 4.8. The wall parameters are chosen as $(a, c_{\mathrm{BW}}) = (0.5, 0.6)$ (blue), (0.6,1.0) (orange), and (0.7,1.0) (green).

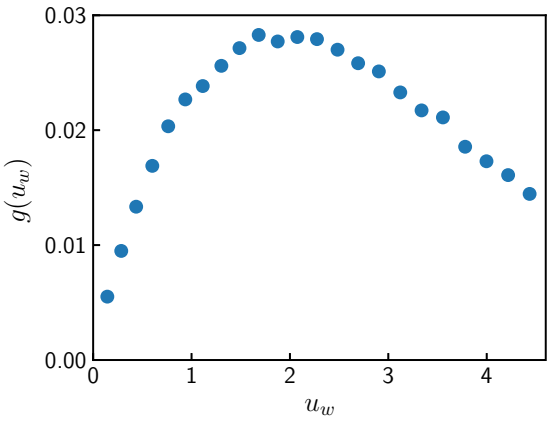

FIG. 4. Plot of $g(u_w)$. The wall parameters and the applied force are chosen as $a = 0.5$, $c_{\mathrm{BW}} = 0.6$, and $0.2 \leqslant f \leqslant 4.8$, which is the same as Fig. 3.

observation in Sec. II C suggests that the microscopic boundary condition is expressed in terms of the shear stress σ^{xz} as a function of the fluid velocity. By noting that the boundary condition is expected to be locally given, we find that the simplest boundary condition is given by

$$\sigma^{xz} = g(u_w), \tag{18}$$

where u_w is the slip velocity extracted from the extrapolated velocity field. In Fig. 4, we plot $g(u_w)$ for the wall with $(a, c_{\mathrm{BW}}) = (0.5, 0.6)$ as f increases from 0.2 to 4.8. We next show that the velocity field $v^x(z)$ is uniquely determined when $g(u_w)$ is given, which is a necessary condition for a boundary condition. By combining (13) with (18), we obtain

$$\eta \frac{U - u_w}{L} = g(u_w). \tag{19}$$

By solving (19), we obtain u_w. Given u_w, $v^x(z)$ is written as

$$v^x(z) = \frac{U - u_w}{L} z + u_w. \tag{20}$$

Therefore, we interpret (18) to be a microscopic boundary condition with $g(u_w)$, the functional form of which is specific to details of the wall and particles.

We remark on some equivalent expressions of (18). We first note that the previous studies [34,42–45] proposed a boundary condition

$$v^x|_{z=0} = b \left. \frac{\partial v^x}{\partial z} \right|_{z=0}, \tag{21}$$

instead of (18), where b corresponds to the slip length. We note that the slip length b may depend on the macroscopic velocity field. By using (10), (11), and (21), we find that the velocity field is expressed in terms of the slip length b as

$$v^x(z) = \frac{U}{L + b}(z + b). \tag{22}$$

By fitting the velocity profile $v^x(z)$ measured in numerical simulations to (22), we obtain the slip length b. The slip length as a function of u_w, $b(u_w)$, is equivalent to the microscopic boundary condition (18). This is because (10) and (18) lead to

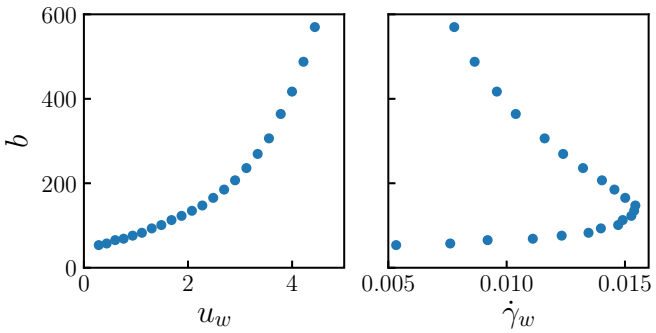

FIG. 5. Slip length as a function of local velocity at the $z = 0$ wall, u_w (left-hand side), and local shear rate at the $z = 0$ wall, $\dot{\gamma}_w$ (right-hand side). The parameter settings are the same as those in Fig. 4.

(21) with

$$b(u_w) = \frac{\eta u_w}{g(u_w)}. \tag{23}$$

As other cases, some previous studies considered the slip length b as a function of shear rate near the wall, $\dot{\gamma}_w$ [37,38,52]. We rewrite (21) in terms of $\dot{\gamma}_w$ as

$$U - \dot{\gamma}_w L = b(\dot{\gamma}_w)\dot{\gamma}_w. \tag{24}$$

If $b(\dot{\gamma}_w)$ is given, then we calculate $\dot{\gamma}_w$ as a function of U and L by solving (24). By recalling $u_w = U - \dot{\gamma}_w L$ and by comparing (18) to (24), we construct $b(\dot{\gamma}_w)$ from $g(u_w)$ as

$$b(\dot{\gamma}_w) = \frac{h(\eta\dot{\gamma}_w)}{\dot{\gamma}_w} \tag{25}$$

where $h(\sigma^{xz})$ is the multivalued function that yields possible values of u_w satisfying (18) for a given σ^{xz}. Equation (25) implies that (18) and (21) with $b(\dot{\gamma}_w)$ are equivalent.

In Fig. 5, we plot b as a function of u_w and $\dot{\gamma}_w$ for the same parameters as Fig. 4. From Figs. 4 and 5, we find that the microscopic boundary condition exhibits a nonlinear behavior. Specifically, Fig. 5 indicates that the slip length depends nonlinearly on u_w or $\dot{\gamma}_w$ and reaches a value more than ten times the system size. This behavior is consistent with some experimental results [1–4]. We remark that the previous numerical simulations [37–39] found a critical shear rate $\dot{\gamma}_c$ at which $b(\dot{\gamma}_w)$ diverges as $\dot{\gamma}_w \to \dot{\gamma}_c$. We conjecture that the results of our simulation are consistent with that of the previous studies. From the right-hand side of Fig. 5, we find that $db(\dot{\gamma}_w)/d\dot{\gamma}_w$ diverges. We consider that the divergence of $b(\dot{\gamma}_w)$ reported in the previous studies corresponds to the divergence of $db(\dot{\gamma}_w)/d\dot{\gamma}_w$ in our simulation. In Appendix B, we demonstrate the correspondence between our simulation and the previous studies by focusing on the scaling law as $\dot{\gamma}_w \to \dot{\gamma}_c$ reported in some studies [37–39].

In Sec. IV C, we shall focus on the nonlinear behavior of the microscopic boundary condition, particularly on the existence of the maximum of $g(u_w)$. The point of $b(u_w)$ that corresponds to the maximum point of $g(u_w)$ is calculated from (23). We find that this point of $g(u_w)$ has a simple graphical interpretation in contrast to that of $b(u_w)$ (see Fig. 4 and the left-hand side of Fig. 5). Also, the corresponding point in $b(\dot{\gamma}_w)$ is the point that the first derivative in $\dot{\gamma}_w$, $db(\dot{\gamma}_w)/d\dot{\gamma}_w$, diverges (see Appendix B). The divergence of $db(\dot{\gamma}_w)/d\dot{\gamma}_w$ provides this point in $b(\dot{\gamma}_w)$ with a simple graphical interpretation. Therefore, we expect that $g(u_w)$ or $b(\dot{\gamma}_w)$ is more useful than $b(u_w)$ for the discussion using graphs. Furthermore, using $b(\dot{\gamma}_w)$ is more mathematically inconvenient than $g(u_w)$ because $b(\dot{\gamma}_w)$ is a two-valued function in $\dot{\gamma}_w$. Therefore, in the reminder of this paper, we use (18) with given $g(u_w)$ as the microscopic boundary condition.

IV. MACROSCOPIC BOUNDARY CONDITION

The microscopic boundary condition is uniquely determined from the microscopic description of the fluid and the wall. That is, $g(u_w)$ is uniquely determined from a given microscopic model. As we change the scale of interest from the microscopic to the macroscopic, we may use the macroscopic boundary condition instead of the microscopic boundary condition. In this section, we study how the macroscopic boundary condition appears, depending on the choice of the scale of interest. For this, we introduce how to choose the scale of interest as a mathematical concept.

A. Choice of the scale of interest

We focus on the L dependence of the velocity field $\bar{v}^x(\bar{z})$ as a function of $\bar{z} \equiv z/L$:

$$\bar{v}^x(\bar{z}) = (U - u_w)\bar{z} + u_w, \tag{26}$$

where we have used (20). We introduce the scaled velocity field by ignoring higher-order terms of $\bar{v}^x(\bar{z})$ in L depending on the scale of interest. The macroscopic boundary condition is determined so that the scaled velocity field is obtained in the standard fluid dynamics. We notice that the macroscopic boundary condition depends on the choice of the terms retained in the scaled velocity field. From (26), we find that the L dependence of $\bar{v}^x(\bar{z})$ is determined from that of U and u_w. This implies that the macroscopic boundary condition is related to the L dependence of u_w. As described in Sec. III B, we obtain u_w by solving (19). Because the L dependence of u_w is connected to the functional form of $g(u_w)$ through (19), we can define the macroscopic boundary condition by the L dependence of u_w or the functional form of $g(u_w)$.

In the remainder of this section, we consider two macroscopic limits in the nonequilibrium steady state that is subjected to the uniform shear flow. In each macroscopic limit, we study the macroscopic boundary condition.

B. Macroscopic boundary condition: quasiequilibrium limit

The first macroscopic limit is the quasiequilibrium limit:

$$L \to \infty, \ U = \text{const}, \ \rho = \text{const}. \tag{27}$$

We focus on the $O(L^{-1})$ terms of the velocity fields $\bar{v}^x(\bar{z})$ as the scale of interest. In this section, $\simeq$ indicates equality up to $o(L^{-1})$ terms.

We define three boundary conditions by noting the L dependence of u_w in the quasiequilibrium limit (27): stick boundary condition $u_w = o(L^{-1})$, partial slip boundary condition $u_w = O(L^{-1})$, and perfect slip boundary condition $Lu_w \to \infty$. Then, the stick boundary condition $u_w = o(L^{-1})$

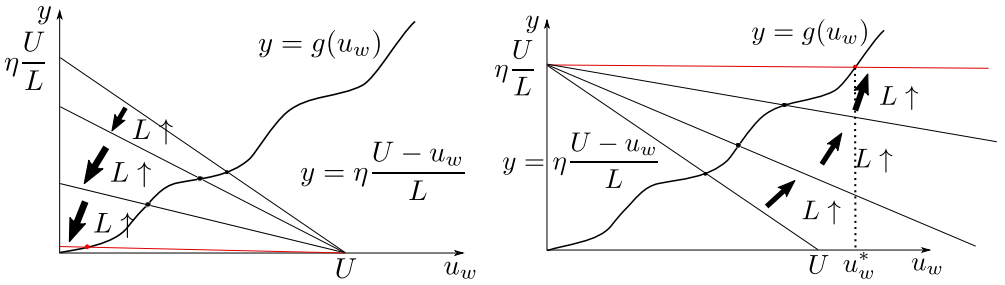

FIG. 6. Schematic graph of $y = g(u_w)$ and $y = \eta(U - u_w)/L$. The intersection of these graphs corresponds to the solution of (19): (a) behavior of the solution in the quasiequilibrium limit and (b) behavior of the solution in the hydrodynamic limit.

implies

$$\bar{v}^x(\bar{z}) \simeq U\bar{z}, \tag{28}$$

which is consistent with the standard stick boundary condition in hydrodynamics.

We consider a relationship between the L dependence of u_w and the functional form of $g(u_w)$. We focus on the case in which the functional form of $g(u_w)$ is given by Fig. 6. In Fig. 6(a), we present the two graphs $y = g(u_w)$ and

$$y = \eta\frac{U - u_w}{L}. \tag{29}$$

The intersection of the two graphs corresponds to the solution of (19). Since U is fixed and $\eta U/L$ approaches 0 in the quasiequilibrium limit (27), the L dependence of the solution is determined by the behavior of $y = g(u_w)$ near $y = 0$ [see Fig. 6(a)]. Then, we consider the three cases of the behavior of $y = g(u_w)$ near $y = 0$.

First, let $g(u_w)$ be expanded around $u_w = 0$ as

$$g(u_w) = g_1 u_w + \frac{1}{2}g_2 u_w^2 + \cdots. \tag{30}$$

We assume $g(0) = 0$ so that the fluid exerts no force on the wall if $u_w = 0$. We consider the case $g_1 \neq 0$. By substituting (30) into (19) and solving for u_w, we obtain

$$u_w \simeq \frac{\eta}{g_1}\frac{U}{L}. \tag{31}$$

As u_w is of order L^{-1}, we find that $g(u_w)$ with $g_1 \neq 0$ corresponds to the partial slip boundary condition.

We next consider the case $g_1 = 0$ and $g_2 \neq 0$. By the similar calculation, we obtain

$$u_w = O(L^{-1/2}) \tag{32}$$

in the quasiequilibrium limit (27). Therefore, we find that $g(u_w)$ with $g_1 = 0$ and $g_2 \neq 0$ corresponds to the perfect slip boundary condition.

Finally, let the first derivative of $g(u_w)$ diverge at $u_w = 0$, as in, for instance,

$$g(u_w) \simeq u_w^a \tag{33}$$

near $u_w = 0$, where $0 < a < 1$. By solving (19), we obtain

$$u_w = O(L^{-1/a}) \tag{34}$$

in the quasiequilibrium limit (27), which corresponds to the stick boundary condition. These results indicate that the boundary condition is determined only by the analyticity of $g(u_w)$ in $u_w = 0$.

We remark that the relationship between the boundary condition defined above and the slip length. We consider the case satisfying the partial slip boundary condition. Since we need to know the linear term of $g(u_w)$ to obtain (31), we rewrite (19) as

$$\left.\frac{\partial v^x}{\partial z}\right|_{z=0} = \left.\frac{1}{b_1}v^x\right|_{z=0} \tag{35}$$

with

$$b_1 \equiv \frac{\eta}{g_1}. \tag{36}$$

We keep in mind that $o(L^{-1})$ terms of $\bar{v}^x(\bar{z})$ are irrelevant for the solutions of the Navier-Stokes equation with boundary condition (35). That is, although the form of the boundary condition (35) is the same as Navier's partial slip boundary condition, i.e., constant slip length, these boundary conditions are different in whether we impose an extent of $\bar{v}^x(\bar{z})$ to be focused. Similarly, we may rewrite the perfect slip boundary condition in the form (35). For example, for $g_1 = 0$ and $g_2 \neq 0$, we rewrite (19) as

$$\left.\frac{\partial v^x}{\partial z}\right|_{z=0} = \left.\frac{1}{b_2}v^x\right|_{z=0} \tag{37}$$

with

$$b_2 \equiv \frac{2\eta}{g_2 v^x|_{z=0}}, \tag{38}$$

which implies that we need to treat the macroscopic-velocity-field-dependent slip length. We note that $b_2 \to \infty$ as $v^x|_{z=0} \to \infty$. This divergence stems from the L dependence of u_w given by (32).

In summary, when we focus on the $O(L^{-1})$ terms of $\bar{v}(\bar{z})$ in the quasiequilibrium limit (27), we impose the stick boundary condition $u_w = 0$, the partial slip boundary condition (35), or the perfect slip boundary condition (37) in accordance with the analyticity of $g(u_w)$ at $u_w = 0$.

C. Macroscopic boundary condition: hydrodynamic limit

The second macroscopic limit is the hydrodynamic limit:

$$L \to \infty, \quad \frac{U}{L} = \text{const}, \quad \rho = \text{const}. \tag{39}$$

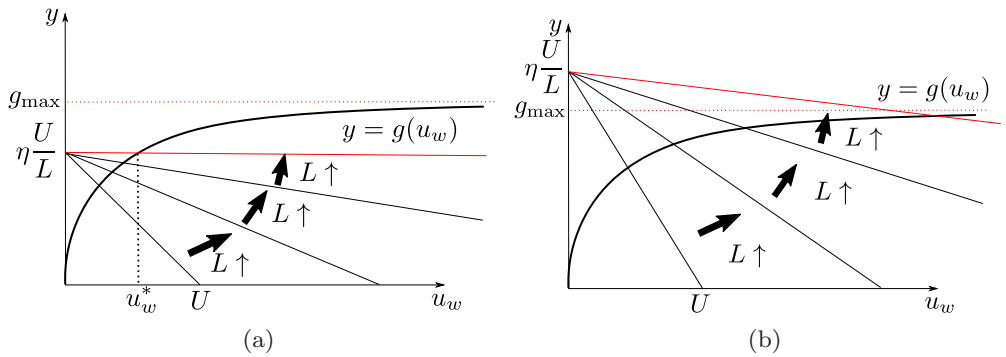

FIG. 7. Schematic graph of $y = g(u_w)$ and $y = \eta(U - u_w)/L$. The intersection of these graphs corresponds to the solution in (19): (a) behavior of the solution for $\eta U/L$ satisfying (44) in the hydrodynamic limit and (b) behavior of the solution for $\eta U/L$ satisfying (45) in the hydrodynamic limit

We focus on the $O(L)$ terms of the velocity fields $\bar{v}^x(\bar{z})$ as the scale of interest. In this section, $\simeq$ indicates equality up to $o(L)$ terms.

We introduce two boundary conditions, stick and perfect slip, in terms of the L dependence of u_w; they are defined respectively as

$$u_w = o(L), \tag{40}$$

and

$$u_w = O(L) \tag{41}$$

in the hydrodynamic limit (39). By recalling (26), we obtain

$$\bar{v}^x(\bar{z}) \simeq U\bar{z} \tag{42}$$

for the stick boundary condition (40). Therefore, we confirm that the stick boundary condition is consistent with the standard stick boundary condition in hydrodynamics.

We focus on a relationship between the L dependence of u_w and the functional form of $g(u_w)$. As in the case of Sec. IV B, we consider the case in which the functional form of $g(u_w)$ is given by Fig. 6. In Fig. 6(b), we present the asymptotic behavior of the solution of (19) in the hydrodynamic limit (39), which is in contrast to Fig. 6(a) in the quasiequilibrium limit (27). By noting that $\eta U/L$ is fixed and U goes to infinity in the hydrodynamic limit (39), we find that u_w approaches finite value u_w^* [see Fig. 6(b)]. u_w^* is given by the solution of the equation

$$\eta\frac{U}{L} = g(u_w^*). \tag{43}$$

When the behavior of $g(u_w)$ is not obtained beyond a linear response regime in u_w, it is difficult to determine a concrete value for u_w^*. Nevertheless, we find u_w^* to be of order L^0 from Fig. 6(b). This corresponds to the stick boundary condition.

Next, we consider the case in which $g(u_w)$ has a maximum $g_{\max}$. We then find that the L dependence of u_w is classified into two cases depending on $\eta U/L$. We consider the functional form of $g(u_w)$ given by Fig. 7. Figure 7 presents the schematic graph of $y = \eta(U - u_w)/L$ and $y = g(u_w)$. $g(u_w)$ has a maximum value $g_{\max}$ at infinity $u_w \to \infty$. The intersection of the two graphs corresponds to the solution of (19). In Fig. 7(a), we present the asymptotic behavior of the solution of (19) for

$$\eta\frac{U}{L} < g_{\max}. \tag{44}$$

From Fig. 7(a), we find that u_w approaches finite value u_w^* independent of L, which corresponds to the stick boundary condition.

In Fig. 7(b), we present the asymptotic behavior of the solution of (19) for

$$\eta\frac{U}{L} \geqslant g_{\max}. \tag{45}$$

From Fig. 7(b), we find that u_w goes to infinity in the hydrodynamic limit (39). $O(L)$ terms of u_w are given by

$$u_w \simeq U - L\frac{g_{\max}}{\eta} \tag{46}$$

in the hydrodynamic limit (39), which corresponds to the perfect slip boundary condition. Note that (46) is rewritten in terms of the shear stress as

$$\sigma^{xz} \simeq g_{\max}. \tag{47}$$

When $g_{\max} = 0$, (47) corresponds to the standard perfect slip boundary condition imposed on the solutions of the Euler equation. These results indicate that the boundary condition depends on the behavior of $g(u_w)$ over the entire range, i.e., the existence of the maximum.

Finally, we consider the case that $g(u_w)$ is given by Fig. 4. We conjecture that the functional form of $g(u_w)$ in Fig. 4 is given by Fig. 8. That is, $g(u_w)$ has a maximum value $g_{\max}$ at $u_w = u_w^{\arg}$ and approaches a constant value $g_\infty \leqslant g_{\max}$ as $u_w \to \infty$.

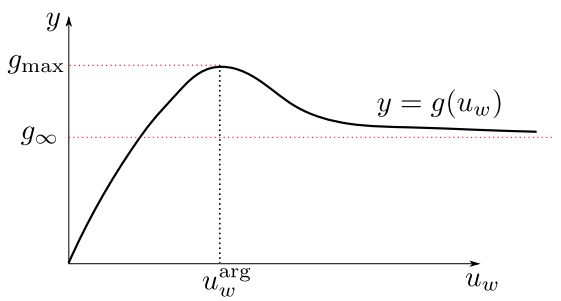

FIG. 8. Schematic image of $g(u_w)$ for the wall $a = 0.5$, $c_{\rm FS} = 0.6$.

By a similar procedure to that in Fig. 7, we find that there are three solutions of (19) depending on $\eta U/L$. First, when the following inequality is satisfied

$$\eta\frac{U}{L} < g_\infty, \tag{48}$$

the solution of (19) approaches finite value u_w^* in the hydrodynamic limit (39), which is given by (43). This implies that the stick boundary condition applies. Second, when

$$g_\infty \leqslant \eta\frac{U}{L} \leqslant g_{\max} \tag{49}$$

holds, (19) has three solutions in the hydrodynamic limit (39). In the hydrodynamic limit (39), the two smaller solutions approach finite values, whereas the largest solution diverges. We consider that all three solutions are physically realizable. In particular, we anticipate that when the external force increases sufficiently slowly from 0 to the appropriate value, the smallest solution is realized. Since the smallest solution approaches a finite value in the hydrodynamic limit (39), this solution corresponds to the stick boundary condition. Finally, when

$$g_{\max} < \eta\frac{U}{L} \tag{50}$$

holds, (19) has one solution, which goes to infinity in the hydrodynamic limit (39). This corresponds to the perfect slip boundary condition, which, in terms of shear stress, is written

$$\sigma^{xz} \simeq g_\infty. \tag{51}$$

In summary, when we focus on the $O(L)$ terms of $\bar{v}(\bar{z})$ in the hydrodynamic limit (39), we impose either the stick boundary condition $u_w = 0$ or the perfect slip boundary condition (47) [or (51)] in accordance with the behavior of $g(u_w)$ over its entire range.

V. SUMMARY

In this paper, we proposed the boundary conditions appropriate for macroscopic hydrodynamics. The key idea of our study was to separate the microscopic boundary condition, which is uniquely determined from the microscopic description of the fluid and the wall, and the macroscopic boundary condition, which depends on the scale of interest. We studied the macroscopic boundary conditions based on the microscopic boundary condition and the macroscopic limits for nonequilibrium steady states.

We used (18) as the microscopic boundary condition, because (18) is the simplest boundary condition satisfying locality. Here, $g(u_w)$ is uniquely determined from the microscopic parameters of the fluid and the wall. We showed that $g(u_w)$ has maximum value for our model using the molecular dynamical simulation.

With ignoring higher terms of $\bar{v}^x(\bar{z})$ in L, we introduced the scaled velocity field that depends on the scale of interest. The macroscopic boundary condition is determined so that the standard fluid dynamics with it gives the scaled velocity field. We proposed two frameworks for determining the macroscopic boundary conditions by defining two macroscopic limits.

The first macroscopic limit is the quasiequilibrium limit. By focusing on the $O(L^{-1})$ terms of the velocity fields $\bar{v}^x(\bar{z})$, we constructed a framework to describe the macroscopic boundary condition comprising three boundary conditions: stick, partial slip, and perfect slip. We showed that the boundary conditions are determined only by the analyticity of $g(u_w)$ at $u_w = 0$. Then, we may classify the boundary conditions in terms of the u_w dependence of the slip length. The stick boundary condition corresponds to $b = 0$. The partial slip boundary condition corresponds to the u_w-independent finite slip length: (35) with (36). The perfect slip boundary condition corresponds to the u_w-dependent slip length: (37) with (38).

The second macroscopic limit is the hydrodynamic limit. By focusing on the $O(L)$ terms of the velocity fields $\bar{v}^x(\bar{z})$, we established a framework for the macroscopic boundary condition that contains two boundary conditions: stick and perfect slip. We showed that the boundary conditions are related to the behavior of $g(u_w)$ over the entire range such as $g_{\max}$ and g_∞. We applied this framework to three cases with $g(u_w)$ of the form given by Figs. 6, 7 and 8. When $g(u_w)$ is given by Fig. 7, the stick boundary condition $u_w = 0$ is realized in the case $\eta U/L < g_{\max}$, whereas the perfect slip boundary condition $\sigma^{xz} = g_{\max}$ is realized in the case $\eta U/L > g_{\max}$.

VI. DISCUSSION

Let us remark on the macroscopic boundary condition for systems with more general geometries in the hydrodynamic limit. The result in Sec. IV C contains the configuration-dependent quantity $\eta U/L$. We conjecture that, by replacing U/L with the shear rate assuming the stick boundary condition, the discussion in Sec. IV C also applies to more general configurations. Based on this conjecture, we obtain the framework in the hydrodynamic limit when $g(u_w)$ is given by Fig. 7. Specifically, we start by assuming the stick boundary condition:

$$\boldsymbol{v}\cdot\boldsymbol{\tau}|_s = 0, \tag{52}$$

where $\boldsymbol{\tau}$ is the tangential vector of the surface and the subscript s represents the evaluation at the surface. When

$$\sigma^{ij}\tau_i n_j|_s \geqslant g_{\max} \tag{53}$$

holds, where the left-hand side is calculated on the stick boundary condition, we apply the perfect boundary condition

$$\sigma^{ij}\tau_i n_j|_s = g_{\max}, \tag{54}$$

where $\boldsymbol{n}$ is the normal vector of the surface.

Our concept of the macroscopic boundary condition may be applied to laboratory experiments. Recently, the slip phenomena were confirmed to be important for nano- and microscale systems [1–4]. One of the reasons why the slip length is regarded as an important quantity in small systems is that the observations are done with the high accuracy for such systems. We consider that the framework of the quasiequilibrium limit is useful to explain phenomena in such small systems, because we can calculate $O(L^{-1})$ terms of u_w/U by using one given parameter g_1 as shown in (31). This is in contrast to the framework established under the hydrodynamic limit, which requires more information about $g(u_w)$ to calculate $O(L^{-1})$ terms of u_w/U as shown in (43). As L is increased with

U fixed and observations are done with lower accuracy, we may ignore even $O(L^{-1})$ terms of the velocity fields $\bar{v}^x(\bar{z})$ in the quasiequilibrium limit. However, when U is sufficiently large, we consider that the slip phenomena are important even for such large systems. In general, when we apply a high shear stress to a fluid, we may observe the slip length of the order of micrometers with the nonlinearity [19,27,37–41]. In such situations, we consider it useful to apply the framework established under the hydrodynamic limit, because it is the simplest framework to extract nonlinear behavior of $g(u_w)$.

As a related study, Priezjev *et al.* reported the shear-rate dependence of slip length in the shear flow of polymer melts past atomically smooth surfaces [38–40]. By using the molecular dynamical simulation, they demonstrated that $g_{\max}$ decreases with increasing the chain length and is nearly independent of the chain length beyond 10 bead-spring units [38]. It was also found that the onset of the nonlinear regime of polymer melts is observed at lower shear rates than that of simple liquids [40]. We expect that the macroscopic boundary condition is useful at high shear rates in these systems. In order to realize a macroscopic slip in realistic systems beyond small systems in a laboratory, it is important to quantitatively evaluate $g_{\max}$, g_∞, and $u_w^{\arg}$ of various type of fluid under realistic settings.

Particularly, for the dilute gases, the slip phenomena have been studied theoretically and experimentally. It was found that when the Knudsen number is on the order of 0.001 or larger, non-negligible slip occurs [57,58]. Recent experiments reported the slip length of 500 nm [59]. The microscopic boundary condition for the gas flow has been discussed by numerous researchers and various slip boundary conditions have been proposed in the literature [57]. They are more complicated than the microscopic boundary condition (18) assumed in this paper. Therefore, it is difficult to apply the results obtained in this paper to the gas flow. However, we consider that the idea to introduce the macroscopic boundary conditions is still useful, because the relatively complicated boundary conditions are expressed as simpler boundary conditions with a few parameters characterizing an amount of slip and nonlinearity. Developing the macroscopic boundary condition for the gas flow is the next problem.

ACKNOWLEDGMENTS

The authors thank A. Yoshimori and Y. Minami for helpful comments. The present study was supported by JSPS KAKENHI Grant No. JP17H01148.

APPENDIX A: EXPRESSION OF MICROSCOPIC DENSITY FIELDS AND MICROSCOPIC CURRENTS

The microscopic mass density field $\hat{\rho}(\boldsymbol{r};\Gamma)$ and the microscopic momentum density field $\hat{\pi}^a(\boldsymbol{r};\Gamma)$ are defined as

$$\hat{\rho}(\boldsymbol{r};\Gamma) \equiv \sum_i m\delta(\boldsymbol{r}-\boldsymbol{r}_i), \tag{A1}$$

$$\hat{\pi}^a(\boldsymbol{r};\Gamma) \equiv \sum_i p_i^a \delta(\boldsymbol{r}-\boldsymbol{r}_i). \tag{A2}$$

We assume that the $z=0$ wall consists of N_w material points and $U_{BW}(\boldsymbol{r}_i)$ is given by (15). Then, $\hat{\pi}^a(\boldsymbol{r},\Gamma)$ satisfies the continuity equation [60–62]

$$\frac{\partial \hat{\pi}^a(\boldsymbol{r};\Gamma_t)}{\partial t} + \frac{\partial \hat{J}^{ab}(\boldsymbol{r};\Gamma_t)}{\partial r^b} = 0 \tag{A3}$$

in $0<z<L$, where the microscopic momentum current $\hat{J}^{ab}(\boldsymbol{r};\Gamma)$ is given by

$$\hat{J}^{ab}(\boldsymbol{r};\Gamma) \equiv \hat{J}_b^{ab}(\boldsymbol{r};\Gamma) + \hat{J}_w^{ab}(\boldsymbol{r};\Gamma) \tag{A4}$$

with

$$\hat{J}_b^{ab}(\boldsymbol{r};\Gamma) \equiv \sum_i \frac{p_i^a p_i^b}{m}\delta(\boldsymbol{r}-\boldsymbol{r}_i) + \sum_{i<j} F_{ij}^a\left(r_i^b - r_j^b\right)D(\boldsymbol{r};\boldsymbol{r}_i,\boldsymbol{r}_j), \tag{A5}$$

$$\hat{J}_w^{ab}(\boldsymbol{r};\Gamma) \equiv \sum_{i=1}^{N}\sum_{j=1}^{N_w} F_{ij}^{wa}\left(r_i^b - q_j^b\right)D(\boldsymbol{r};\boldsymbol{r}_i,\boldsymbol{q}_j), \tag{A6}$$

where we have used the definition of the following quantities:

$$D(\boldsymbol{r};\boldsymbol{r}_i,\boldsymbol{r}_j) \equiv \int_0^1 d\xi\,\delta(\boldsymbol{r}-\boldsymbol{r}_i-(\boldsymbol{r}_j-\boldsymbol{r}_i)\xi), \tag{A7}$$

$$F_{ij}^a \equiv -\frac{\partial V_{\rm FF}(|\boldsymbol{r}_i-\boldsymbol{r}_j|)}{\partial r_i^a}, \tag{A8}$$

$$F_{ij}^{wa} \equiv -\frac{\partial V_{\rm BW}(|\boldsymbol{r}_i-\boldsymbol{q}_j|)}{\partial r_i^a}. \tag{A9}$$

In the numerical simulation, the averaged density fields are calculated by spatially and temporally averaging the microscopic density fields [e.g., (7)]. These quantities are expressed as

$$\rho(z) = \frac{1}{\tau}\int_0^\tau dt \frac{1}{L_xL_y\Delta z}\sum_i m\Theta(\boldsymbol{r}_i(t);\mathcal{R}_z), \tag{A10}$$

$$\pi^a(z) = \frac{1}{\tau}\int_0^\tau dt \frac{1}{L_xL_y\Delta z}\sum_i p_i^a\Theta(\boldsymbol{r}_i(t);\mathcal{R}_z), \tag{A11}$$

$$J_b^{ab}(z) = \frac{1}{\tau}\int_0^\tau dt \frac{1}{L_xL_y\Delta z}\left[\sum_i \frac{p_i^a(t)p_i^b(t)}{m}\Theta(\boldsymbol{r}_i(t);\mathcal{R}_z) + \sum_{i<j} F_{ij}^a(t)\left(r_i^b(t)-r_j^b(t)\right)D(\boldsymbol{r}_i(t),\boldsymbol{r}_j(t);\mathcal{R}_z)\right], \tag{A12}$$

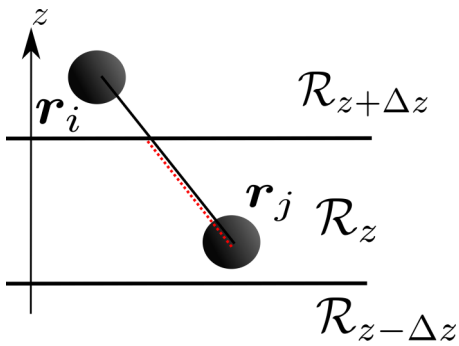

FIG. 9. Schematic image of $D(\boldsymbol{r}_i,\boldsymbol{r}_j;\mathcal{R}_z)$. $D(\boldsymbol{r}_i,\boldsymbol{r}_j;\mathcal{R}_z)$ is given as the ratio of black line and red dotted line.

and

$$J_w^{ab}(z) = \frac{1}{\tau}\int_0^\tau dt \frac{1}{L_x L_y \Delta z}\left[\sum_{i=1}^{N}\sum_{j=1}^{N_w} F_{ij}^{wa}(t)\big(r_i^b(t) - r_j^b(t)\big) D(\boldsymbol{r}_i(t), \boldsymbol{r}_j(t); \mathcal{R}_z)\right] \tag{A13}$$

with

$$\mathcal{R}_z = [0, L_x] \times [0, L_y] \times \left[z - \frac{\Delta z}{2}, z + \frac{\Delta z}{2}\right], \tag{A14}$$

$$\Theta(\boldsymbol{r}; \mathcal{R}_z) = \begin{cases} 0 & \boldsymbol{r} \notin \mathcal{R}_z, \\ 1 & \boldsymbol{r} \in \mathcal{R}_z, \end{cases} \tag{A15}$$

and

$$D(\boldsymbol{r}_i, \boldsymbol{r}_j; \mathcal{R}_z) = \begin{cases} 0 & \boldsymbol{r}_i \in \mathcal{R}_{z-\Delta z} \text{ and } \boldsymbol{r}_j \in \mathcal{R}_{z-\Delta z}, \\ z_{jd}/z_{ij} & \boldsymbol{r}_i \in \mathcal{R}_{z-\Delta z} \text{ and } \boldsymbol{r}_j \in \mathcal{R}_z, \\ (z_{ij} - z_{id} - z_{ju})/z_{ij} & \boldsymbol{r}_i \in \mathcal{R}_{z-\Delta z} \text{ and } \boldsymbol{r}_j \in \mathcal{R}_{z+\Delta z}, \\ z_{id}/z_{ij} & \boldsymbol{r}_i \in \mathcal{R}_z \text{and } \boldsymbol{r}_j \in \mathcal{R}_{z-\Delta z}, \\ 1 & \boldsymbol{r}_i \in \mathcal{R}_z \text{ and } \boldsymbol{r}_j \in \mathcal{R}_z, \\ z_{iu}/z_{ij} & \boldsymbol{r}_i \in \mathcal{R}_z \text{and } \boldsymbol{r}_j \in \mathcal{R}_{z+\Delta z}, \\ (z_{ij} - z_{jd} - z_{iu})/z_{ij} & \boldsymbol{r}_i \in \mathcal{R}_{z+\Delta z} \text{and } \boldsymbol{r}_j \in \mathcal{R}_{z-\Delta z}, \\ z_{ju}/z_{ij} & \boldsymbol{r}_i \in \mathcal{R}_{z+\Delta z} \text{and } \boldsymbol{r}_j \in \mathcal{R}_z, \\ 0 & \boldsymbol{r}_i \in \mathcal{R}_{z+\Delta z} \text{and } \boldsymbol{r}_j \in \mathcal{R}_{z+\Delta z}, \end{cases} \tag{A16}$$

where $r_{ij} = |\boldsymbol{r}_i - \boldsymbol{r}_j|$, $z_{ij} = |z_i - z_j|$, $z_{id} = |z_i - (z - \Delta z/2)|$ and $z_{iu} = |z_i - (z + \Delta z/2)|$. Here we give the graphical interpretation of $D(\boldsymbol{r}_i, \boldsymbol{r}_j; \mathcal{R}_z)$ in Fig. 9.

APPENDIX B: SCALING LAW AT HIGH SHEAR RATES

In Sec. III, we gave an example for which $g(u_w)$ has a maximum (see Fig. 4). We conjecture that the functional form of $g(u_w)$ is given by Fig. 8. With this conjecture, we considered the macroscopic boundary condition in Sec. IV C. As explained in Sec. III B, the previous studies [37–39] reported the behavior that $b(\dot\gamma_w)$ diverges at $\dot\gamma_w \to \dot\gamma_c$ and provided the scaling law for simple liquids

$$\frac{b(\dot\gamma_w)}{b^*} = \left(1 - \frac{\dot\gamma_w}{\dot\gamma_c}\right)^{-\frac{1}{2}} \tag{B1}$$

near the critical value $\dot\gamma_c$, where b^* is a constant. In this Appendix, we show that, under some assumptions, $g(u_w)$ of the type shown in Fig. 8 satisfies the scaling law (B1). That is, our simulations are consistent with the previous studies in terms of scaling behavior.

As U increases from 0, u_w increases and g goes up a slope of $g(u_w)$ to reach $g_{\max}$ (see Fig. 8). We assume that $u_w^{\arg}$ is sufficiently large so that u_w cannot reach $u_w^{\arg}$ within numerical simulations. Then, we restrict ourselves to $u_w < u_w^{\arg}$. Since $g(u_w)$ is a bijective function in $u_w < u_w^{\arg}$, we rewrite (25) in terms of the inverse function of $g(u_w)$ as

$$g^{-1}(\eta\dot\gamma_w) = b(\dot\gamma_w)\dot\gamma_w. \tag{B2}$$

We introduce the critical shear rate $\dot\gamma_c$ by

$$\dot\gamma_c = \frac{g_{\max}}{\eta}. \tag{B3}$$

By noting that $g^{-1}(\eta\dot\gamma_c) = u_w^{\arg}$, we obtain

$$\left.\frac{dg^{-1}(\eta\dot\gamma_w)}{d\dot\gamma_w}\right|_{\dot\gamma_c} = \left(\left.\frac{dg(u_w)}{du_w}\right|_{u_w^{\arg}}\right)^{-1} = \infty. \tag{B4}$$

From (B2) and (B4), we find that $\dot\gamma_c$ is the point for which the first derivative of $b(\dot\gamma_w)$ in $\dot\gamma_w$, $db(\dot\gamma_w)/d\dot\gamma_w$ diverges.

If we regard $u_w^{\arg}$ as infinity, then we conjecture that $g(u_w)$ can be expanded around $u_w = u_w^{\arg}$ as

$$g(u_w) = g_{\max} - \left(\frac{1}{u_w^4}\frac{d^2g}{du_w^2}\right)_{u_w^{\arg}} \frac{1}{u_w^2} + \cdots. \tag{B5}$$

Equation (B5) means that $g(u_w)$ has no singular point near $u_w = u_w^{\arg}$. By using (B2), (B3), and (B5), we find that $b(\dot\gamma_w)$ is given by

$$b(\dot\gamma_w) \simeq \frac{1}{\dot\gamma_c\sqrt{g_{\max}}}\sqrt{\left(\frac{1}{u_w^4}\frac{d^2g}{du_w^2}\right)_{u_w^{\arg}}}\left(1 - \frac{\dot\gamma_w}{\dot\gamma_c}\right)^{-\frac{1}{2}} \tag{B6}$$

near $\dot\gamma_w = \dot\gamma_c$. Equation (B6) implies that $b(\dot\gamma_w)$ diverges at $\dot\gamma_w = \dot\gamma_c$ following the scaling law (B1). Thus, we conclude that the results of our simulation are consistent with the previous studies in terms of scaling behavior.

[1] C. Neto, D. R. Evans, E. Bonaccurso, H.-J. Butt, and V. S. J. Craig, Rep. Prog. Phys. **68**, 2859 (2005).

[2] E. Lauga, M. P. Brenner, and H. A. Stone, in *Handbook of Experimental Fluid Dynamics*, edited by J. Foss, C. Tropea, and A. Yarin (Springer, New York, 2007).

[3] B.-Y. Cao, J. Sun, M. Chen, and Z.-Y. Guo, Int. J. Mol. Sci. **10**, 4638 (2009).

[4] L. Bocquet and E. Charlaix, Chem. Soc. Rev. **39**, 1073 (2010).

[5] O. I. Vinogradova, Int. J. Miner. Process. **56**, 31 (1999).

[6] R. Pit, H. Hervet, and L. Leger, Phys. Rev. Lett. **85**, 980 (2000).

[7] V. S. J. Craig, C. Neto, and D. R. M. Williams, Phys. Rev. Lett. **87**, 054504 (2001).
[8] D. C. Tretheway and C. D. Meinhart, Phys. Fluids **14**, L9 (2002).
[9] J. Baudry, E. Charlaix, A. Tonck, and D. Mazuyer, Langmuir **17**, 5232 (2001).
[10] Y. Zhu and S. Granick, Phys. Rev. Lett. **87**, 096105 (2001).
[11] Y. Zhu and S. Granick, Phys. Rev. Lett. **88**, 106102 (2002).
[12] E. Bonaccurso, M. Kappl, and H.-J. Butt, Phys. Rev. Lett. **88**, 076103 (2002).
[13] C. Cottin-Bizonne, S. Jurine, J. Baudry, J. Crassous, F. Restagno, and E. Charlaix, Eur. Phys. J. E **9**, 47 (2002).
[14] J. T. Cheng and N. Giordano, Phys. Rev. E **65**, 031206 (2002).
[15] S. Granick, Y. Zhu, and H. Lee, Nat. Mater. **2**, 221 (2003).
[16] C. Neto, V. S. J. Craig, and D. R. M. Williams, Eur. Phys. J. E **12**, 71 (2003).
[17] O. I. Vinogradova and G. E. Yakubov, Langmuir **19**, 1227 (2003).
[18] D. Lumma, A. Best, A. Gansen, F. Feuillebois, J. O. Rädler, and O. I. Vinogradova, Phys. Rev. E **67**, 056313 (2003).
[19] C.-H. Choi, K. J. A. Westin, and K. S. Breuer, Phys. Fluids **15**, 2897 (2003).
[20] Jae-Hie J. Cho, B. M. Law, and F. Rieutord, Phys. Rev. Lett. **92**, 166102 (2004).
[21] C. Cottin-Bizonne, B. Cross, A. Steinberger, and E. Charlaix, Phys. Rev. Lett. **94**, 056102 (2005).
[22] P. Joseph and P. Tabeling, Phys. Rev. E **71**, 035303(R) (2005).
[23] P. Huang, J. S. Guasto, and K. S. Breuer, J. Fluid Mech. **566**, 447 (2006).
[24] P. Huang and K. S. Breuer, Phys. Fluids **19**, 028104 (2007).
[25] C. D. F. Honig and W. A. Ducker, Phys. Rev. Lett. **98**, 028305 (2007).
[26] A. Maali, T. Cohen-Bouhacina, and H. Kellay, Appl. Phys. Lett. **92**, 053101 (2008).
[27] U. Ulmanella and C. M. Ho, Phys. Fluids **20**, 101512 (2008).
[28] A. Steinberger, C. Cottin-Bizonne, P. Kleimann, and E. Charlaix, Phys. Rev. Lett. **100**, 134501 (2008).
[29] C. Cottin-Bizonne, A. Steinberger, B. Cross, O. Raccurt, and E. Charlaix, Langmuir **24**, 1165 (2008).
[30] O. I. Vinogradova, K. Koynov, A. Best, and F. Feuillebois, Phys. Rev. Lett. **102**, 118302 (2009).
[31] S. A. Gupta, H. D. Cochran, and P. T. Cummings, J. Chem. Phys. **107**, 10316 (1997).
[32] J.-L. Barrat and L. Bocquet, Phys. Rev. Lett. **82**, 4671 (1999).
[33] M. Cieplak, J. Koplik, and J. R. Banavar, Phys. Rev. Lett. **86**, 803 (2001).
[34] L. Bocquet and J.-L. Barrat, Phys. Rev. E **49**, 3079 (1994).
[35] J.-L. Barrat and L. Bocquet, Faraday Discuss. **112**, 119 (1999).
[36] C. Cottin-Bizonne, J.-L. Barrat, L. Bocquet, and E. Charlaix, Nat. Mater. **2**, 237 (2003).
[37] P. A. Thompson and S. M. Troian, Nature **389**, 360 (1997).
[38] N. V. Priezjev and S. M. Troian, Phys. Rev. Lett. **92**, 018302 (2004).
[39] N. V. Priezjev, Phys. Rev. E **80**, 031608 (2009).
[40] N. V. Priezjev, Phys. Rev. E **82**, 051603 (2010).
[41] A. Martini, H.-Y. Hsu, N. A. Patankar, and S. Lichter, Phys. Rev. Lett. **100**, 206001 (2008).
[42] C. L. M. H. Navier, Mem. Académie des Inst. Sciences Fr. **6**, 389 (1823).
[43] H. Lamb, *Hydrodynamics* (Dover, New York, 1932), pp. 594–616.
[44] J. Happel and H. Brenner, *Low Reynolds Number Hydrodynamics: With Special Applications to Particulate Media* (Springer, New York, 1983).
[45] O. I. Vinogradova, Langmuir **11**, 2213 (1995).
[46] J. C. Maxwell, Philos. Trans. R. Soc. London **170**, 231 (1879).
[47] L. D. Landau and E. M. Lifshitz, *Fluid Mechanics* (Pergamon Press, Oxford, 1959).
[48] C. Y. Wang, Phys. Fluids **15**, 1114 (2003).
[49] A. Jabbarzadeh, J. D. Atkinson, and R. I. Tanner, Phys. Rev. E **61**, 690 (2000).
[50] I. V. Ponomarev and A. E. Meyerovich, Phys. Rev. E **67**, 026302 (2003).
[51] N. V. Priezjev and S. M. Troian, J. Fluid Mech. **554**, 25 (2006).
[52] N. V. Priezjev, J. Chem. Phys. **127**, 144708 (2007).
[53] A. Niavarani and N. V. Priezjev, Phys. Rev. E **81**, 011606 (2010).
[54] D. M. Huang, C. Sendner, D. Horinek, R. R. Netz, and L. Bocquet, Phys. Rev. Lett. **101**, 226101 (2008).
[55] R. S. Voronov, D. V. Papavassiliou, and L. L. Lee, Ind. Eng. Chem. Res. **47**, 2455 (2008).
[56] H. Watanabe, M. Suzuki, and N. Ito, Prog. Theor. Phys. **126**, 203 (2011).
[57] S. Colin, Microfluid. Nanofluid. **1**, 268 (2005).
[58] A. Maali, S. Colin, and B. Bhushan, Nanotechnology **27**, 374004 (2016).
[59] D. Seo and W. A. Ducker, Phys. Rev. Lett. **111**, 174502 (2013).
[60] H. Spohn, *Large Scale Dynamics of Interacting Particles, Texts and Monographs in Physics* (Springer-Verlag, Heidelberg, 1991).
[61] S. P. Das, *Statistical Physics of Liquids at Freezing and Beyond* (Cambridge University Press, Cambridge, England, 2011).
[62] S.-i. Sasa, Phys. Rev. Lett. **112**, 100602 (2014).